

The origin of slow Alfvénic solar wind at solar minimum

D. Stansby^{1*}, L. Matteini², T. S. Horbury¹, D. Perrone^{3,1}, R. D’Amicis⁴, L. Berčič^{2,5}

¹*Department of Physics, Imperial College London, London, SW7 2AZ, UK*

²*LESIA, Observatoire de Paris, Université PSL, CNRS, Sorbonne Université,*

Univ. Paris Diderot, Sorbonne Paris Cité, 5 place Jules Janssen, 92195 Meudon, France

³*ASI - Italian Space Agency, via del Politecnico snc, 00133 Rome, Italy*

⁴*INAF - IAPS, Via Fosso del Cavaliere 100, Rome, Italy*

⁵*Physics and Astronomy Department, University of Florence, Via Giovanni Sansone 1, I-50019 Sesto Fiorentino, Italy*

19 July 2022

ABSTRACT

Although the origins of slow solar wind are unclear, there is increasing evidence that at least some of it is released in a steady state on over-expanded coronal hole magnetic field lines. This type of slow wind has similar properties to the fast solar wind, including a high degree of Alfvénicity. In this study a combination of proton, alpha particle, and electron measurements are used to investigate the kinetic properties of a single interval of slow Alfvénic wind at 0.35 AU. It is shown that this slow Alfvénic interval is characterised by high alpha particle abundances, pronounced alpha-proton differential streaming, strong proton beams, and large alpha to proton temperature ratios. These are all features observed consistently in the fast solar wind, adding evidence that at least some Alfvénic slow solar wind also originates in coronal holes. Observed differences between speed, mass flux, and electron temperature between slow Alfvénic and fast winds are explained by differing magnetic field geometry in the lower corona.

Key words: Sun: heliosphere – solar wind.

1 INTRODUCTION

The solar wind is an ionised plasma flowing at large speeds from the surface of the Sun to the edge of the Heliosphere. Although the density, speed, and temperature of the solar wind are all highly variable, it is possible to identify categories of solar wind with distinct properties. The most clearly defined category is that with the highest speeds, typically called the fast solar wind. Comparison between remote observations and in situ measurements show that fast solar wind originates in large coronal holes spanning over 60° in angular width (Krieger et al. 1973; Nolte et al. 1976; Cranmer 2009; Garton et al. 2018).

In contrast the solar sources of wind with slow and intermediate speeds are varied and still not entirely clear (e.g. see the review of Abbo et al. 2016). There are, however, multiple lines of evidence that a significant fraction of the slow solar wind also originates in coronal holes. One of the defining features of fast solar wind is a lack of variance in number density, velocity, and temperature, aside from pure Alfvénic fluctuations (Belcher & Davis 1971; Bame et al. 1977). A steady background state with superimposed Alfvén waves is also observed in situ in a large amount of the slower solar wind at all stages of the solar cycle (D’Amicis & Bruno 2015;

Stansby et al. 2019b), implying that close to the Sun it may also be heated and released into the heliosphere in a steady state manner on open field lines.

One significant difference between the regions of coronal holes that produce slow and fast winds is the magnetic field geometry in the corona. The amount of magnetic field expansion alters the location of the critical point where the plasma becomes supersonic (Cranmer 2005), which in turn alters the effects of heating processes. If the majority of heating happens below the critical point, the speed is not significantly affected, whereas significant heating above the critical point is expected to increase the speed (Leer & Holzer 1980). Because rapidly diverging magnetic fields have a higher critical point, more energy is deposited before the wind becomes supersonic, thus resulting in slower wind speeds (Levine et al. 1977; Leer & Holzer 1980; Wang & Sheeley 1991).

These theoretical predictions agree well with an observed anti-correlation between solar wind speed at 1 AU and the amount of super-radial expansion the magnetic field undergoes close to the Sun (Wang & Sheeley 1990, 2006; Suzuki 2006; Fujiki et al. 2015). Statistically the smallest coronal holes, with the highest magnetic field expansions, produce wind with the slowest speeds (Nolte et al. 1976; Hofmeister et al. 2018; Garton et al. 2018), which has been verified on a case by case basis using magnetic field map-

* E-mail: david.stansby14@imperial.ac.uk

Table 1. Start and end times for selected intervals. All data are taken from Helios 1.

Category	Start time (UT)	End time (UT)
Fast	1975/03/13 12:00	1975/03/16 12:00
Slow Alfvénic	1975/03/23 00:00	1975/03/24 16:00
Slow non-Alfvénic	1975/03/25 14:00	1975/03/26 00:00

pings from spacecraft to the solar surface (Wang et al. 2009; Wang 2017). In addition, case studies at 1 AU show that the slow Alfvénic wind contains similar heavy ion composition (D’Amicis et al. 2018), and similar alpha to proton abundance ratios (Ohmi et al. 2004) as fast solar wind, reinforcing a probable similar solar origin. These previous studies have shown that the bulk properties of the slow Alfvénic wind are consistent with the theory that it originates in open field lines rooted in coronal holes.

If this theory is true, one would expect the processes occurring as the solar wind is heated and accelerated to be similar in both the fast and slow Alfvénic wind, and thus expect similar features to be found in the velocity distribution functions in both types of wind. The kinetic features of fast solar wind have been extensively characterised: it contains a proton beam population (Feldman et al. 1973, 1993), large alpha particle to proton temperature ratios (Marsch et al. 1982a; Stansby et al. 2019c), magnetic field aligned proton-alpha particle streaming (Marsch et al. 1982a; Neugebauer et al. 1996), and large alpha to proton abundance ratios (Aellig et al. 2001; Kasper et al. 2007). Marsch et al. (1982b) and D’Amicis et al. (2018) have shown that at 1 AU both fast and slow Alfvénic winds tend to have isotropic proton distributions, but the other features have yet to be measured in slow Alfvénic wind.

In this paper we provide the first observations of these kinetic features in both slow and fast Alfvénic winds. Some of these features are destroyed by the time the solar wind has propagated to 1 AU, necessitating the use of data from the Helios mission, which measured the solar wind from 0.3 – 1 AU. Three intervals are studied, initially identified by Stansby et al. (2019b) as a) typical fast solar wind, b) Alfvénic slow solar wind, and c) non-Alfvénic slow solar wind. Our comparison of both the bulk and kinetic features of fast and slow Alfvénic intervals shows that the slow Alfvénic period most likely originated from a small, over-expanded coronal hole.

2 DATA

The data used here were measured by the *Helios* mission, which consisted of two spacecraft in heliocentric orbits between 0.3 and 1 AU (Porsche 1977). The first perihelion pass of *Helios 1* during solar minimum was used, from which three periods were chosen as representative examples of fast, slow Alfvénic and slow non-Alfvénic wind. The intervals are listed in table 1 and shown later in figure 2, and were chosen to contain continuous alpha particle measurements and to be long enough to build up a statistical characterisation of each interval.

Particle data were measured by the E1 set of instruments, consisting of electrostatic analysers for both ions and

electrons (Schwenn et al. 1975). Magnetic field data were measured by both the E2 and E3 fluxgate magnetometers (Musmann et al. 1975; Scearce et al. 1975). Where possible magnetic field data from E2 were used, with E3 data as a fallback. Although data gaps are frequent, the particle data is available at a maximum cadence of 40.5 seconds, and magnetic field measurements are averaged over the time taken to build up each individual particle distribution function.

Alpha particle parameters were calculated using the bi-Maxwellian fitting routine described in Stansby et al. (2019c), with minor modifications to adapt the fitting to work well in both slow and fast solar winds¹. Proton temperatures and velocities are bi-Maxwellian fits to the proton core from the dataset of Stansby et al. (2018)². Electron core parameters were obtained using the method presented in Berčič et al. (2019), also calculated with a bi-Maxwellian fitting routine. Example ion energy spectra for each interval, along with their corresponding proton and alpha particle fits, are shown in figure 1, demonstrating that the fitting works well in all types of wind. Energy per charge units (measured directly by the instrument) can be converted to velocity for a given particle species by

$$\sqrt{\frac{E}{q}} = v\sqrt{\frac{m}{2q}} \quad (1)$$

where m and q are the particle mass and electromagnetic charge respectively. Because of their increased charge to mass ratio, in these plots alpha particles appear at $\sqrt{E/q}$ values a factor of $\sqrt{2}$ higher than protons travelling at the same speed.

In figure 1 some differences are already apparent between the three types of wind. The fast (top panel) and slow Alfvénic wind (bottom left panel) show a similar structure, with a proton core population, an additional proton beam population visible as a hump in the measured distribution to the right of the proton core fit, and an alpha particle distribution which is wider and therefore significantly hotter than the proton distribution. In contrast the slow non-Alfvénic wind (bottom right panel) has no obvious proton beam, and a much thinner alpha particle distribution than the other types of wind.

For each species, the fitted parameters are number density (n_i), velocity (\mathbf{v}_i), and temperatures perpendicular and parallel to the local magnetic field ($T_{i\perp}, T_{i\parallel}$). The subscript i is substituted as p for protons, α for alpha particles, or e for electrons.

As shown above, an additional proton beam population can also be present that is not captured by bi-Maxwellian fits, and can comprise more than 10% of the core density (Feldman et al. 1973; Marsch et al. 1982b; Stansby et al. 2018). For this reason, the proton number density used here is a numerical integration containing contributions from both the core and the beam populations, taken from the original *Helios* plasma dataset³.

¹ The updated fitting routine can be found at <https://github.com/dstansby/alphafit>, and the newly calculated parameters at <https://doi.org/10.5281/zenodo.3258337>

² Available at <https://doi.org/10.5281/zenodo.1009506>.

³ Available at <ftp://cdaweb.gsfc.nasa.gov/pub/data/helios/helios1/merged/>

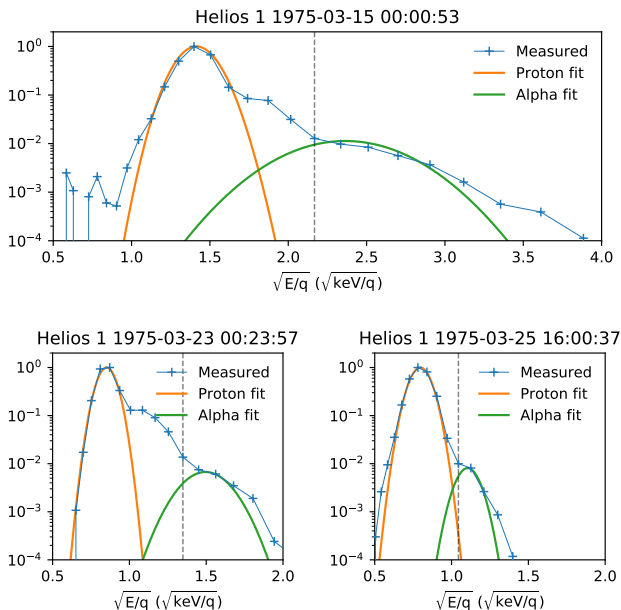


Figure 1. Example energy spectra (blue crosses) measured in each type of solar wind. Top panel shows fast wind, bottom left slow Alfvénic wind, and bottom right slow non-Alfvénic wind. The solid angle integrated bi-Maxwellian fits are shown for protons (orange line) and alpha particles (green line). The vertical grey line shows the dividing line between measurements dominated by protons (to the left) and those dominated by alpha particles (to the right).

Aside from these basic properties, some derived parameters are used later, which are defined as follows:

- The Alfvén speed is

$$v_A = \frac{|\mathbf{B}|}{\sqrt{\mu_0 \rho}} \quad (2)$$

where $\rho = \sum_i n_i m_i$ is the total mass density of the plasma.

- The proton beam fraction is

$$\frac{n_b}{n_p} = \frac{n_p - n_{pc}}{n_p} \quad (3)$$

where n_{pc} is the proton core number density calculated from bi-Maxwellian fits and n_p is the total proton density calculated as a numerical moment.

- The cross helicity is defined as (Bruno & Carbone 2013)

$$\sigma_c = 2 \frac{\langle \mathbf{v} \cdot \mathbf{b} \rangle}{\langle |\mathbf{v}|^2 + |\mathbf{b}|^2 \rangle} \quad (4)$$

and is calculated in the same manner as Stansby et al. (2019b). $\mathbf{v} = \mathbf{v}_p - \mathbf{v}_{p0}$ are the proton velocity fluctuations in the Alfvén wave frame, \mathbf{v}_{p0} is chosen to maximise the value of $|\sigma_c|$, and $\mathbf{b} = v_A (\mathbf{B}/|\mathbf{B}|)$ is the magnetic field in velocity units. The time averages denoted by $\langle \rangle$ are taken over all points in non-overlapping 20 minute windows.

3 RESULTS

Figure 2 presents an overview of the first perihelion pass of Helios 1 in early 1975. This shows a typical solar minimum

structure in the ecliptic plane, with several fast coronal hole streams interspersed with slower wind speed periods.

The intervals listed in table 1 are shown with coloured vertical bands in figure 2, and are examples of fast (grey), slow Alfvénic (blue) and slow non-Alfvénic (red) wind. Note that the slow Alfvénic stream begins after clear discontinuities in proton number density and temperature, and is clearly distinct from the trailing edge of the preceding high speed stream. Both the fast and slow Alfvénic periods have very high Alfvénicities, with $|\sigma_c| > 0.9$, whereas the non-Alfvénic wind is characterised by a large scatter of $|\sigma_c|$ values between 0 and 1.

Figure 3 shows histograms of various parameters in each type of wind, using the same interval colour coding as figure 2. Panel a) shows the proton radial velocity, making clear that the slow Alfvénic wind has significantly slower speeds (~ 400 km/s) than the fast wind (~ 600 km/s). Panel b) shows the alpha particle flux, normalised to the proton flux ($v_{\alpha r} n_{\alpha} / v_{pr} n_p$). Note that the relative flux is plotted instead of the relative abundance, since the abundance is not conserved if the alpha particle and proton velocities change, whereas the flux is conserved (Hollweg 1974; Wang 2008). At these distances the relative fluxes and abundances are similar however, due to relatively similar proton and alpha particle radial speeds. The slow Alfvénic wind has similar relative alpha particle fluxes to the fast solar wind (~ 0.05), whereas the non-Alfvénic wind has significantly smaller fluxes, as shown previously (for another interval) by Ohmi et al. (2004). Panel c) shows the proton number density flux, normalised to radial distance (ie. particles per second per solid angle). The slow Alfvénic wind has a flux around twice that of the fast wind, and the non-Alfvénic wind has large fluxes around four times the fast wind flux. Panel d) shows the electron perpendicular temperature, which in the slow Alfvénic wind (0.2 MK) is twice that of the fast wind (0.1 MK), but slightly cooler than the non-Alfvénic wind (0.25 MK). Panel e) shows the proton beam fraction. In both the fast and non-Alfvénic wind the beam fraction is around 10%, whereas in the slow Alfvénic wind the beam fraction is significantly higher at 25%. Panel f) shows the alpha particle streaming speed. In agreement with previous studies (e.g. Marsch et al. 1982a; Neugebauer et al. 1996) alphas stream at a significant fraction of the Alfvén speed in the fast solar wind, and the alpha particles also stream at a slightly smaller but still significant fraction in the slow Alfvénic wind. The non-Alfvénic wind has an average proton-alpha drift speed of zero, which may be due to its relatively high collisionality (due to a high density and low temperature). Finally, panels g) and h) respectively show the proton and alpha particle temperature anisotropy. The non-Alfvénic wind is isotropic for both particle populations, again most likely due to a high collisionality. The sense of temperature anisotropy is the same in the fast and slow Alfvénic winds, with $T_{\perp} > T_{\parallel}$ for protons but $T_{\perp} < T_{\parallel}$ for alpha particles, however the proton temperature anisotropy is weaker in the slow Alfvénic wind compared to the fast wind (see also Stansby et al. 2019b). Note that at least in the fast wind, these features in alpha particle temperatures are not observable at 1 AU, due to the effect of plasma micro-instabilities on the evolution of alpha particle temperatures (Stansby et al. 2019c).

Figure 4 shows the joint distributions of proton and al-

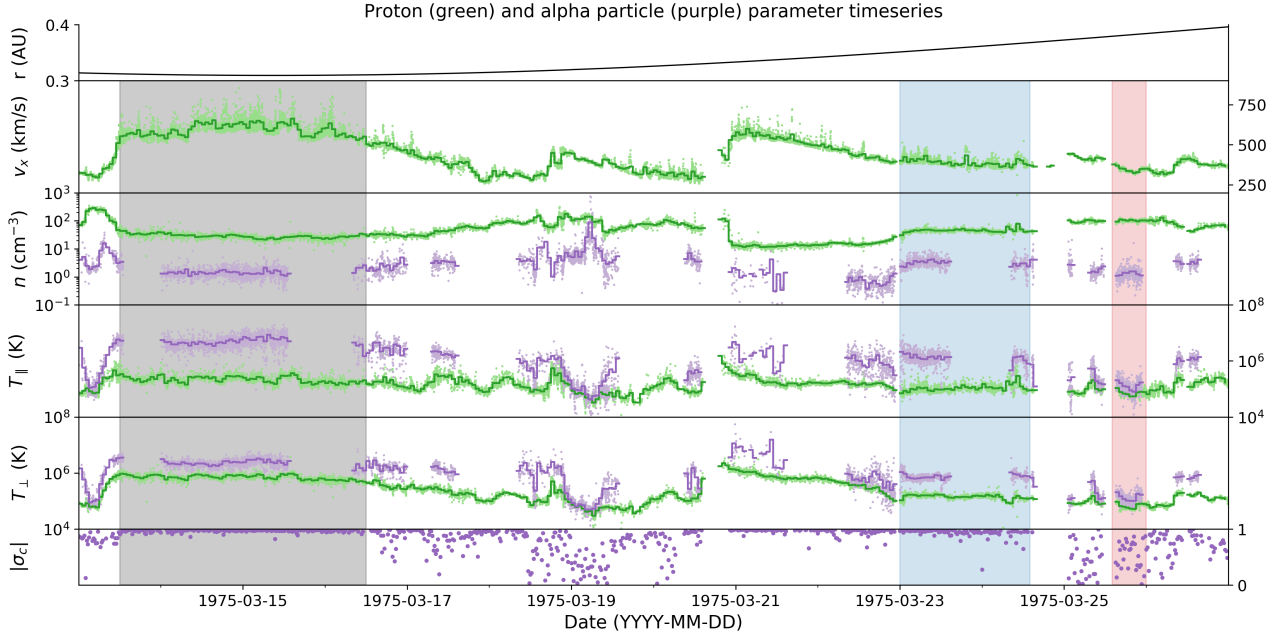


Figure 2. Proton (green) and alpha particle (purple) parameter timeseries from the first perihelion pass of Helios 1. From top to bottom: heliocentric distance, radial velocity, number density, parallel temperature, perpendicular temperature, and absolute cross helicity. In the middle 4 panels 40.5 second cadence measurements are shown with light dots, and hourly averaged parameters with dark lines.

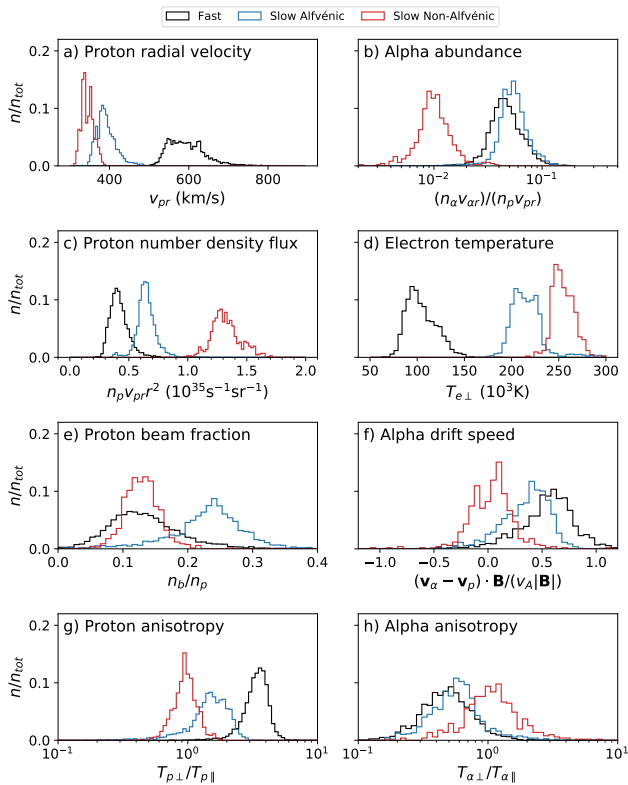


Figure 3. Histograms of various parameters in the three different intervals, normalised to the total number of data points in each interval.

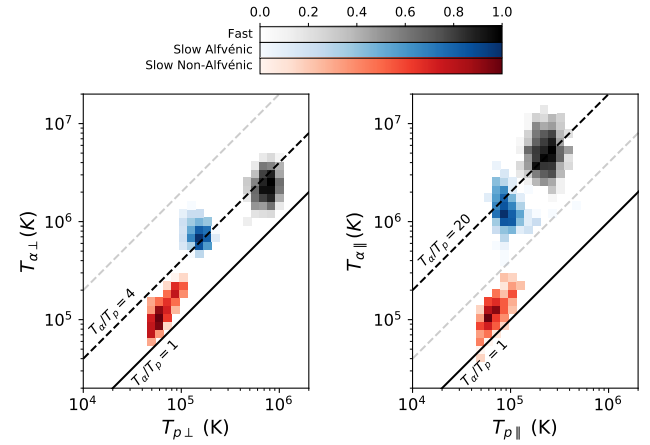


Figure 4. Joint distribution of magnetic field perpendicular (left hand panel) and parallel (right hand panel) proton and alpha particle temperatures in three types of solar wind. Distributions are normalised to the maximum bin value.

alpha particle temperatures in each of the three types of wind, with the same colour coding as figure 3. The non-Alfvénic wind has $T_{\alpha\perp} \approx T_{\alpha\parallel} \approx 10^5$ K. The similarity in proton and alpha particle temperatures here may again be due to the non-Alfvénic wind's relatively high collisionality. On the other hand the slow Alfvénic wind has an order of magnitude larger alpha particle temperatures of $\sim 10^6$ K. The alpha to proton temperature ratios are similar in the fast and slow Alfvénic wind, in both the perpendicular ($T_{\alpha\perp} \approx 4T_{p\perp}$) and parallel ($T_{\alpha\parallel} \approx 20T_{p\parallel}$) directions.

4 DISCUSSION

The slow Alfvénic solar wind has similar alpha to proton number density fluxes as the fast solar wind (figure 3, panel b). Because alpha particles are heavier than protons, they require extra forces above those that accelerate the protons acting on them in order to avoid gravitational settling reducing their abundance to significantly less than the photospheric abundance (Hansteen et al. 1994; Basu & Antia 1995; Asplund et al. 2009). Our results suggest that similar mechanisms driving these enhanced Helium fluxes are active in both the fast and slow Alfvénic solar winds, but not in the non-Alfvénic slow wind. More specifically, there must be mechanisms other than Coulomb friction, which alone would make the alpha abundance very sensitive to the proton number density flux (Geiss et al. 1970), in contrast to these observations.

In addition, the slow Alfvénic and fast winds both have similar proton-alpha drift speeds (figure 3, panel f) and alpha to proton temperature ratios (figure 4). Proposed mechanisms to impart these properties include second order effects of Alfvén waves (Hollweg 1974; Chang & Hollweg 1976), ion cyclotron wave acceleration (Hollweg & Isenberg 2002), or reconnection jets (Feldman et al. 1993, 1996). Although the observations presented here cannot distinguish between these different proposals, they suggest that similar mechanisms are active in both the fast and slow Alfvénic wind.

The slow Alfvénic wind shows some differences to the fast wind however; it has slower speeds (figure 3, panel a), higher mass fluxes (figure 3, panel c), higher electron temperatures (figure 3, panel d), and lower overall proton and alpha temperatures (figure 4). These observations agree with the idea that both the fast and slow Alfvénic solar wind were produced on open field lines rooted in coronal holes, but with varying magnetic field geometries in the lower corona. In particular, the amount the magnetic field expands in the low corona (up to $2.5r_{\odot}$), the footpoint magnetic field strength, and the magnetic field inclination at the solar surface are all thought to be important in shaping the properties of coronal hole wind (Suess et al. 1984; Wang & Sheeley 1990; Bravo & Stewart 1997; Suzuki 2006; Pinto et al. 2016; Réville & Brun 2017).

The amount of magnetic field expansion sets the location of the critical point where the plasma becomes supersonic, with higher expansion factors resulting in higher Alfvénic points (Cranmer 2005; Cranmer et al. 2007). This in turn alters the effects of heating processes. If heating happens whilst the wind is sub-Alfvénic, the mass flux is increased but the speed is not expected to be significantly affected; on the other hand, heating the wind whilst it is supersonic is expected to leave the mass flux unchanged but to increase the flow speed (Leer & Holzer 1980; Wang et al. 2009). This leads to more energy being deposited below the critical point for rapidly diverging magnetic fields, thus resulting in slower speeds but increased mass fluxes (Levine et al. 1977; Leer & Holzer 1980; Wang & Sheeley 1991), precisely as observed.

The lower ion temperatures in the slow Alfvénic wind agree with previous statistical observations of a positive correlation between proton bulk speed and both proton (Elliott et al. 2012) and alpha particle (Thieme et al. 1989) temper-

atures, and also agree with observations at 1 AU of the slow Alfvénic wind at solar maximum (D’Amicis et al. 2018). Although the mechanisms behind this relation are still not clear, it is reproducible in steady state models of the solar wind (Cranmer et al. 2007; Pinto & Rouillard 2017; Usmanov et al. 2018).

The higher electron temperatures in the slow Alfvénic wind with respect to the fast wind are also in agreement with previous observational in situ results, showing an anti-correlation between proton bulk speed and electron temperature at solar minimum (Marsch et al. 1989; Pilipp et al. 1990). This anti-correlation may be a reflection of coronal electron temperature variations, with higher T_e in slower wind, agreeing with remote sensing measurements showing relatively low electron temperatures in coronal holes (see section 12 of Del Zanna & Mason 2018, and references therein). This variation can also be reproduced in steady state solar wind models (Oran et al. 2015).

These T_e variations observed at solar minimum are in contrast to the solar maximum case of D’Amicis et al. (2018), who inferred from heavy ion composition that slow Alfvénic wind had a similar coronal electron temperature to the fast wind. To investigate possible differences between solar minimum and solar maximum, heavy ion data measured at 1 AU by the SWICS instrument (Gloeckler et al. 1998)⁴ on board the *Advanced Composition Explorer* (ACE) can be used as a proxy for coronal electron temperature (e.g. Geiss et al. 1995; Landi et al. 2012).

Figure 5 shows the relation between solar wind speed and heavy ion charge state ratios measured by SWICS during both a solar maximum and a solar minimum. At solar maximum the fastest solar wind has enhanced O^{7+}/O^{6+} and C^{6+}/C^{4+} charge state ratios compared to solar minimum (see also Lepri et al. 2013). At maximum, enhanced charge state ratios in the fast wind (especially in C^{6+}/C^{4+}) imply that fast and slow Alfvénic wind have similar coronal electron temperatures, as concluded by D’Amicis et al. (2018). In contrast, at minimum there is a large difference between charge state ratios at low and high speeds, implying a much cooler coronal electron temperature in the fast wind. This agrees with our in situ electron temperature results (figure 3, panel d).

5 CONCLUSIONS

We have presented a detailed case study comparison between the kinetic properties of protons and alpha particles in the fast, slow Alfvénic, and slow non-Alfvénic solar wind using data taken by Helios 1 during its first perihelion passage. The similarity in alpha particle abundance, alpha to proton temperature ratio, and alpha particle drift speed in the slow Alfvénic and fast winds adds additional evidence that some slow Alfvénic wind originates in coronal holes, similarly to the fast solar wind. The differences in speed, mass flux, and electron temperatures between the slow Alfvénic and fast solar wind are explained by different magnetic field geometries in the low corona: the slower wind is released on magnetic

⁴ Data available at https://cdaweb.gsfc.nasa.gov/pub/data/ace/swics/level_2_cdaweb/swi_h2/

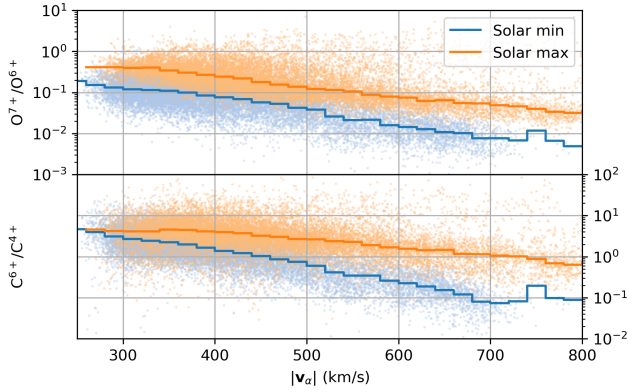


Figure 5. Heavy ion charge state ratios as a function of solar wind speed for a solar maximum (orange, 2000 - 2003 inclusive) and a solar minimum (blue, 2007 - 2010 inclusive). Light dots show individual measurements, and solid lines show medians in 20 km/s bins.

field lines that undergo over-expansion that modifies the effects of coronal heating and acceleration processes.

An obvious next step would be performing a magnetic field connectivity analysis (e.g. Neugebauer et al. 1998) to determine if the observing spacecraft was really connected to a small coronal hole at the time of measurement. Unfortunately, to our knowledge, there are no magnetic field or extreme ultraviolet images of the Sun available for the interval studied in 1975. However, *Parker Solar Probe* (PSP, Fox et al. 2016) is predicted to have been connected to a small coronal hole during its first closest approach to the Sun (Riley et al. 2019). Having taken in situ measurements of the solar wind down to 0.15 AU, PSP will allow measurement of the kinetic features of solar wind un-ambiguously emitted from a small coronal hole during solar minimum.

ACKNOWLEDGEMENTS

The authors thank Roberto Bruno for helpful discussions, and Marcia Neugebauer for comments and suggestions that significantly contributed to the results and discussion. D. Stansby, T. S. Horbury, and D. Perrone were supported by STFC grant ST/N000692/1. This work was supported by the Programme National PNST of CNRS/INSU co-funded by CNES.

The authors are grateful to the *Helios* and ACE instrument teams for making the data used in this study publicly available. Data were retrieved using Heliopy v0.8.0 (Stansby et al. 2019a) and processed using astropy v3.2.1 (The Astropy Collaboration et al. 2018). Figures were produced using Matplotlib v3.1.1 (Hunter 2007).

Code to reproduce the figures presented in this paper is available at <https://github.com/dstansby/publication-code>.

REFERENCES

Abbo L., et al., 2016, *Space Science Reviews*, 201, 55

- Aellig M. R., Lazarus A. J., Steinberg J. T., 2001, *Geophysical Research Letters*, 28, 2767
- Asplund M., Grevesse N., Sauval A. J., Scott P., 2009, *Annual Review of Astronomy and Astrophysics*, 47, 481
- Bame S. J., Asbridge J. R., Feldman W. C., Gosling J. T., 1977, *Journal of Geophysical Research*, 82, 1487
- Basu S., Antia H. M., 1995, *Monthly Notices of the Royal Astronomical Society*, 276, 1402
- Belcher J. W., Davis L., 1971, *Journal of Geophysical Research*, 76, 3534
- Berčić L., Maksimović M., Landi S., Matteini L., 2019, *Monthly Notices of the Royal Astronomical Society*, 486, 3404
- Bravo S., Stewart G. A., 1997, *The Astrophysical Journal*, 489, 992
- Bruno R., Carbone V., 2013, *Living Reviews in Solar Physics*, 10, 1
- Chang S. C., Hollweg J. V., 1976, *Journal of Geophysical Research (1896-1977)*, 81, 1659
- Cranmer S. R., 2005, arXiv:astro-ph/0506508
- Cranmer S. R., 2009, *Living Reviews in Solar Physics*, 6, 3
- Cranmer S. R., van Ballegooijen A. A., Edgar R. J., 2007, *The Astrophysical Journal Supplement Series*, 171, 520
- D’Amicis R., Bruno R., 2015, *The Astrophysical Journal*, 805, 84
- D’Amicis R., Matteini L., Bruno R., 2018, *Monthly Notices of the Royal Astronomical Society*, 483, 4665
- Del Zanna G., Mason H. E., 2018, *Living Reviews in Solar Physics*, 15, 5
- Elliott H. A., Henney C. J., McComas D. J., Smith C. W., Vasquez B. J., 2012, *Journal of Geophysical Research: Space Physics*, 117
- Feldman W. C., Asbridge J. R., Bame S. J., Montgomery M. D., 1973, *Journal of Geophysical Research*, 78, 2017
- Feldman W. C., Gosling J. T., McComas D. J., Phillips J. L., 1993, *Journal of Geophysical Research: Space Physics*, 98, 5593
- Feldman W. C., Barraclough B. L., Phillips J. L., Wang Y.-M., 1996, *Astronomy and Astrophysics*, 316, 355
- Fox N. J., et al., 2016, *Space Science Reviews*, 204, 7
- Fujiki K., Tokumaru M., Iju T., Hakamada K., Kojima M., 2015, *Solar Physics*, 290, 2491
- Garton T. M., Murray S. A., Gallagher P. T., 2018, *The Astrophysical Journal*, 869, L12
- Geiss J., Hirt P., Leutwyler H., 1970, *Solar Physics*, 12, 458
- Geiss J., Gloeckler G., Von Steiger R., 1995, *Space Science Reviews*, 72, 49
- Gloeckler G., et al., 1998, *Space Science Reviews*, 86, 497
- Hansteen V. H., Leer E., Holzer T. E., 1994, *The Astrophysical Journal*, 428, 843
- Hofmeister S. J., Veronig A., Temmer M., Vennertstrom S., Heber B., Vršnak B., 2018, *Journal of Geophysical Research: Space Physics*, 123, 1738
- Hollweg J. V., 1974, *Journal of Geophysical Research (1896-1977)*, 79, 1357
- Hollweg J. V., Isenberg P. A., 2002, *Journal of Geophysical Research: Space Physics*, 107, SSH 12
- Hunter J. D., 2007, *Computing in Science & Engineering*, 9, 90
- Kasper J. C., Stevens M. L., Lazarus A. J., Steinberg J. T., Ogilvie K. W., 2007, *The Astrophysical Journal*, 660, 901
- Krieger A. S., Timothy A. F., Roelof E. C., 1973, *Solar Physics*, 29, 505
- Landi E., Alexander R. L., Gruesbeck J. R., Gilbert J. A., Lepri S. T., Manchester W. B., Zurbuchen T. H., 2012, *The Astrophysical Journal*, 744, 100
- Leer E., Holzer T. E., 1980, *Journal of Geophysical Research: Space Physics*, 85, 4681
- Lepri S. T., Landi E., Zurbuchen T. H., 2013, *The Astrophysical Journal*, 768, 94
- Levine R. H., Altschuler M. D., Harvey J. W., 1977, *Journal of*

- Geophysical Research, 82, 1061
- Marsch E., Mühlhäuser K.-H., Rosenbauer H., Schwenn R., Neubauer F. M., 1982a, *Journal of Geophysical Research*, 87, 35
- Marsch E., Mühlhäuser K.-H., Schwenn R., Rosenbauer H., Pilipp W., Neubauer F. M., 1982b, *Journal of Geophysical Research*, 87, 52
- Marsch E., Pilipp W. G., Thieme K. M., Rosenbauer H., 1989, *Journal of Geophysical Research: Space Physics*, 94, 6893
- Musmann G., Neubauer F. M., Maier A., Lammers E., 1975, *Raumfahrtforschung*, 19, 232
- Neugebauer M., Goldstein B. E., Smith E. J., Feldman W. C., 1996, *Journal of Geophysical Research: Space Physics*, 101, 17047
- Neugebauer M., et al., 1998, *Journal of Geophysical Research: Space Physics*, 103, 14587
- Nolte J. T., et al., 1976, *Solar Physics*, 46, 303
- Ohmi T., Kojima M., Tokumaru M., Fujiki K., Hakamada K., 2004, *Advances in Space Research*, 33, 689
- Oran R., et al., 2015, *The Astrophysical Journal*, 806, 55
- Pilipp W. G., Miggenrieder H., Mühlhäuser K.-H., Rosenbauer H., Schwenn R., 1990, *Journal of Geophysical Research*, 95, 6305
- Pinto R. F., Rouillard A. P., 2017, *The Astrophysical Journal*, 838, 89
- Pinto R. F., Brun A. S., Rouillard A. P., 2016, *Astronomy & Astrophysics*, 592, A65
- Porsche H., 1977, *Journal of Geophysics*, 42, 551
- Réville V., Brun A. S., 2017, *The Astrophysical Journal*, 850, 45
- Riley P., Downs C., Linker J. A., Mikic Z., Lionello R., Caplan R. M., 2019, *The Astrophysical Journal*, 874, L15
- Scearce C., Cantarano S., Ness N., Mariani F., Terenzi R., Burlaga L., 1975, *Raumfahrtforschung*, 19, 237
- Schwenn R., Rosenbauer H., Miggenrieder H., 1975, *Raumfahrtforschung*, 19, 226
- Stansby D., Salem C., Matteini L., Horbury T., 2018, *Solar Physics*, 293, 155
- Stansby D., et al., 2019a, Heliopython/Heliopy: HelioPy 0.8.0, Zenodo, doi:10.5281/zenodo.3256541, <https://zenodo.org/record/3256541>
- Stansby D., Horbury T. S., Matteini L., 2019b, *Monthly Notices of the Royal Astronomical Society*, 482, 1706
- Stansby D., Perrone D., Matteini L., Horbury T. S., Salem C. S., 2019c, *Astronomy & Astrophysics*, 623, L2
- Suess S. T., Wilcox J. M., Hoeksema J. T., Henning H., Dryer M., 1984, *Journal of Geophysical Research: Space Physics*, 89, 3957
- Suzuki T. K., 2006, *The Astrophysical Journal*, 640, L75
- The Astropy Collaboration et al., 2018, *The Astronomical Journal*, 156, 123
- Thieme K. M., Marsch E., Rosenbauer H., 1989, *Journal of Geophysical Research*, 94, 2673
- Usmanov A. V., Matthaeus W. H., Goldstein M. L., Chhiber R., 2018, *The Astrophysical Journal*, 865, 25
- Wang Y.-M., 2008, *The Astrophysical Journal*, 683, 499
- Wang Y.-M., 2017, *The Astrophysical Journal*, 841, 94
- Wang Y.-M., Sheeley Jr. N. R., 1990, *The Astrophysical Journal*, 355, 726
- Wang Y.-M., Sheeley N. R., 1991, *The Astrophysical Journal*, 372, L45
- Wang Y.-M., Sheeley N. R., 2006, *The Astrophysical Journal*, 653, 708
- Wang Y.-M., Ko Y.-K., Grappin R., 2009, *The Astrophysical Journal*, 691, 760